Whole Mantle SH Velocity Model Constrained by Waveform Inversion Based on 3D Born Kernels

Nozomu Takeuchi
Earthquake Research Institute, University of Tokyo,
Yayoi 1-1-1, Bunkyo-ku, Tokyo 113-0032, Japan
takeuchi@eri.u-tokyo.ac.jp

October 20, 2008

SUMMARY

A whole mantle SH velocity model is obtained by using a unique data set and techniques. Body and surface waveforms including major and multi-orbit phases are used as a data set and are inverted by using 3D Born kernels. The resultant model, SH18CE, reveals the different natures of the two major upwelling systems: the strong low velocity anomalies beneath Africa extend for more than 1000 km from the core-mantle boundary (CMB), whereas those beneath the Pacific are restricted to 300-400 km from the CMB. The results also show the variable natures of stagnant slabs on the 670 discontinuity around Japan: the depths of the strongest high velocity anomalies within the stagnant slabs are different region by region, which is consistent with the detailed delay time tomography model in this area.
Keywords: Global seismology, Inversion, Seismic structure, Tomography, Direct Solution Method

1 Introduction

Seismic structure models have been improved over the last two decades by using various data sources and techniques. Though a wide variety of models exists, but they can be classified into two main categories: models obtained by using short period data (hereafter referred to as short wavelength models) and those obtained using broadband data (referred to as long wavelength models).

The short wavelength models are obtained generally by using travel time data of body wave phases. Because of the accuracy of phase identification and picking, the initial P travel times are most extensively used, and most short wavelength models are P models. They are strong in resolving fine structures and have succeeded in revealing, for example, the fate of subducting slabs (e.g., van der Hilst *et al.* 1997; Bijwaard *et al.* 1998). Although efforts have been made to use later phases, the reliability of their travel time data is in question. Most of the models obtained so far are relatively weak in resolving, for example, the oceanic regions where coverage of direct P waves is poor.

The long wavelength models are obtained generally by using higher quality waveform data. Because of the higher sensitivity of surface waveforms to the S velocity structure and the well isolated later body wave phases in the transverse component of body waveforms, most long wavelength models are S models. Secondary data (such as the body wave travel times, phase velocity of surface waves, and splitting functions of modes of free oscillations) are frequently

extracted from the waveforms and are inverted (e.g., Ritsema *et al.* 1999; Masters *et al.* 2000; Grand 2002; Montelli *et al.* 2004). To fully exploit information included in the waveform data, a waveform inversion (e.g., Mégnin & Romanowicz 2000; Panning & Romanowicz 2006) or a joint inversion of the secondary data and waveform data (e.g., Gu *et al.* 2001, 2003) is conducted. These procedures are strong in resolving the long wavelength features of global lateral heterogeneities but are relatively weak in resolving fine structures.

In this study, a long wavelength S model is obtained by using a unique data set and waveform inversion techniques. The obtained model is expected to include information not included in the previous models for the following two reasons. First, as described below, the data set used more extensively includes later body waveforms. In many of the previous studies, only body waveforms before the surface wave arrival were used as the primary body wave data source. On the other hand, this study attempts to use all waveform data whose phase and amplitude are reasonably close to those of the synthetic seismograms. The resultant data set includes major and multi-orbit body waveforms, and the data coverage is expected to be improved.

Second, the waveform inversion in this study computes accurate 3D Born kernels. In the previous studies, to save required CPU time, approximations were used in computing kernels: the pioneering work by Woodhouse & Dziewonski (1984) introduced the path average approximation, while Li & Tanimoto (1993) and Li & Romanowicz (1995) expanded this approach to improve the accuracy of body wave kernels. All these methods have limitations in that they use great circle approximation and neglect part of the contributions from modal couplings. On the other hand, the method used in this study does not incorporate any approximations other than truncations of basis in computing Born kernels and thus rigorously considers off-great circle effects and modal couplings. The waveform inversions based on 3D Born kernels were conducted only for surface wave data (e.g., Hara 2004), and this is the first time the 3D Born kernels have been used for whole mantle tomography (except for preliminary studies by, for example, Takeuchi & Kobayashi 2004). The main drawback of this approach is the requirement of huge computational resources. However, it is now feasible if we use an efficient computational method, the Direct Solution Method (e.g., Geller & Ohminato 1994; Takeuchi *et al.* 2000), and the Earth Simulator (http://www.es.jamstec.go.jp/esc/eng/ES/index.html). The Direct Solution Method is based on the accurate discretization method (Geller & Takeuchi 1995; Takeuchi & Geller 2003), and the accuracy of synthetic seismograms is improved by about thirty times without increasing the required CPU time (e.g., Cummins *et al.* 1994; Takeuchi *et al.* 1996; Kawai *et al.* 2006).

In this paper, we first confirm that the overall features of the obtained model are consistent with those of previous studies, and then focus on the detailed structure. Two notable detailed features are found in the obtained model: the structure in the upwelling regions and the structure of the stagnant slabs around Japan. The consistency between these features and the previous studies is also shown.

2 Data Set and Inversion Methods

2.1 Data Set

Figure 1 shows the method used to choose the data set employed in this study. The basic idea is to include all useful data regardless of the type of seismic phase. We apply three different bandpass filters (200-400 s, 100-200 s, and 50-100 s) to a single trace and compare them to the corresponding synthetic seismograms. The length of the time series is about 4 hours from the centroid time. We compute the Hilbert transform of both observed and synthetic seismograms to compute their phase and amplitude as a function of time. We extract time windows in which the residual of the phase is within 75° and the amplitude ratio is between 0.4-2.5. The threshold for phase is determined by considering the limitation of the Born approximation employed in

this inversion: we cannot represent phase perturbations greater than 90°. The reason why we allow relatively larger perturbations in the amplitude is their relatively small impact on the norm which we want to minimize in waveform inversions. This criterion discards data with high S/N ratios but very large perturbations; however, note that we apply three different filters to a single trace and, even if we reject such data for shorter period components, we have reasonable chances to adopt them for longer period components. We adopt only larger time windows (more than 400, 200, and 100 sec for filtered traces with corner periods of 200-400, 100-200, and 50-100 sec, respectively, if it is before the arrival of $G1$, and more than 1000, 500, and 250 sec, otherwise) as a data set. The reason why we choose only larger time windows is described below.

The example in Figure 1 shows the waveform data (shown in the red lines) and synthetic seismograms (shown in the green lines) of the station OBN (the epicentral distance is 59.9°) for the Japan Sea event on 07/21/94 (the centroid depth is 489.1 km and the moment magnitude is $M_{\rm W} = 7.3$). The boxes show the time windows in which data are adopted as a data set. For data in periodic ranges of surface waves or overtones (say, periods longer than 100 sec), data from major and multi-orbit phases are often used. However, for data in periodic ranges of body waves (say, periods shorter than 100 sec), only data from primary body wave phases (e.g., S, ScS, SS, and ScS_2) are usually used. Body waveforms after the surface wave arrival (after the arrival of $G1$ in the case of the transverse component) were not well utilized. This is probably because the later body waves are often contaminated with various unidentified phases and the waveforms can be seriously distorted. In this study, we consider that such distortion is not a serious problem when the time duration of reasonable coincidence between the data and the synthetics is sufficiently long. This is based on the idea that the amplitude and the phase of the observed waveforms with serious distortion are seldom in close agreement with those of the synthetic seismograms over a long period of time. Figure 1c shows that this criterion effectively chooses data from useful later body wave phases such as ScS_3, ScS_4, major SSS, major $SSSSS$ and many other later phases (including multi-orbit phases after $G3$) which were not extensively used in the previous studies (note that these later phases are included not only for deep events but also for shallow events as well). The waveform data used in making the data set are the transverse components of data from IRIS/USGS, IRIS/IDA, IRIS/CDSN, and GEOSCOPE for 191 events ($M_{\rm W} \geq 6.5$ between 1991-2004). The resultant data set consists of $103,074$ time windows in $15,262$ independent traces.

Through the adoption of such later body waveforms, the data set in this study is expected to be improved in terms of data coverage. Figure 2 shows the sensitivity distribution at the CMB for the data set used in this study (left) and the data set which excludes data arriving after $G1$ in the body wave periodic range of 50-100 sec (right). The sensitivity is computed by the sum of the square norm of the kernels for the weighted data set. The explicit definition is given by eqs. (3), (11), and (13) in Takeuchi & Kobayshi (2004). When we exclude later body phases, the sensitivity is poor beneath Africa, the Indian Sea, and the South Pacific. However, by fully including later body phases, we can improve the coverage in these areas. For the coverage at the CMB, data from multiple reverberation phases between the surface and the CMB (such as ScS_3, ScS_4, and ScS_5) should contribute to the improvement of coverage.

These results suggest that the model obtained by this study is constrained by a different data source compared to those in the previous studies. Figure 8 in Megnin & Romanowicz (2000) shows ray coverage of ScS and $S_{\rm diff}$ which are major sources to resolve the structure of the lowermost mantle in most of the previous studies. The sensitivity distribution for the data set without data arriving after G1 (Fig. 2, right) is moderately similar to the coverage of ScS. This is because, as will be described later, we determine weighting factors for each trace and do not define different weighting factors for each wavepacket. This means that we do not enhance wavepackets with smaller amplitudes such as $S_{\rm diff}$ and that wavepackets with larger amplitudes such as ScS better contribute to the sensitivity. Megnin & Romanowicz (1999)

showed that weighting for individual wavepackets to enhance $S_{\rm diff}$ can improve the resolution in the lowermost mantle. In contrast we improve the resolution by fully incorporating later phases. The merit of this approach is that it avoids enhancing noise in the data, which degrades the accuracy of the obtained models.

2.2 Initial Model and Model Parameters

The anisotropic PREM (Dziewonski & Anderson 1981) and the Harvard CMT solutions (with ramped source time functions) are used as the initial model of the Earth's structure and the source parameters, respectively. The bathemetry, the Conrad and Moho topographies given by CRUST2.0 (Bassin *et al.* 2000), along with the hydrostatic ellipticity, are taken into account. The crustal and ellipticity corrections are made using the method of Woodhouse (1980). Application of the more accurate method of Takeuchi (2005) is a subject for future research.

Because we use the transverse component of the waveform data, the data is sensitive primarily to the SH velocity structure. In this study, we perturbed only the elastic constants and fixed the other parameters (the density, the quality factors, and the source parameters). Because we neglected the effects of the toroidal-spheroidal couplings and assumed that only the toroidal component contributes to the transverse component (as some previous studies have assumed), only the elastic constants N and L (notations follow those of Love, 1927) can be resolved. Here, we define the model parameters δm_α by the expansion

$$\frac{\delta N\left(r,\theta,\phi\right)}{N^{(0)}(r)} = \sum_{\alpha} \delta m_\alpha \, X^{(k)}(r)\, Y^{(st)}\left(\theta,\phi\right), \tag{1}$$

and assume the scaling relation

$$\frac{\delta L\left(r,\theta,\phi\right)}{L^{(0)}(r)} = \frac{\delta N\left(r,\theta,\phi\right)}{N^{(0)}(r)}, \tag{2}$$

where α is a pointer to the triplet of indices (k,s,t); r, θ, and ϕ denote the radius, the colatitude, and the longitude, respectively; $N^{(0)}(r)$ and $L^{(0)}(r)$ are N and L of the PREM, respectively; $\delta N\left(r,\theta,\phi\right)$ and $\delta L\left(r,\theta,\phi\right)$ are the perturbations of the elastic constants N and L with respect to those of the PREM, respectively; $X^{(k)}$ is the k-th vertically dependent function described below, and $Y^{(st)}$ is the spherical harmonics with the angular order s and the azimuthal order t.

The linear spline functions are used as $X^{(k)}(r)$ in eq. (1) to expand the heterogeneities in the mantle. The linear spline functions have 13 nodes in the mantle: 6 of these nodes are in the upper mantle, 1 is on the 670 km discontinuity, and 6 are in the lower mantle. The node locations are at 24.4 (Moho), 70 , 160, 280, 400, 530, 670, 920, 1210, 1550, 1940, 2390, and 2891 (CMB) km depths, respectively. To correct the crustal structure, the boxcar function, which has unit value only at depths in the crust and is zero otherwise, is used as $X^{(k)}(r)$. We thus use 14 functions as the vertically dependent part of the basis functions in eq. (1). The angular order of $Y^{(st)}$ in eq. (1) is between 0-18, and we use 361 functions as the horizontally dependent part of the basis functions. The total number of model parameters is thus $5,054$.

2.3 Inversion Methods

The inversion method used in this study follows the standard least square procedures with smoothness constraints. In most geophysical inverse problems, we first assume the dependency between the model parameters $\boldsymbol{\delta}\mathbf{m}$ and the observed data $\boldsymbol{\delta}\mathbf{d}$ by the linear equation

$$\boldsymbol{\delta}\mathbf{d} = \mathbf{A}\,\boldsymbol{\delta}\mathbf{m}, \tag{3}$$

where $\mathbf{A}$ is the Born kernel given by

$$A_{ij} = \frac{\partial d_i}{\partial m_j}. \tag{4}$$

In this study we use the model parameters defined in eq. (1) as $\boldsymbol{\delta}\mathbf{m}$ and use the weighted residuals between the observed waveform data and the synthetic seismograms for the initial model (with crustal and ellipticity corrections) as $\boldsymbol{\delta}\mathbf{d}$. Weighting is defined in a similar fashion as in Woodhouse & Dziewonski (1984): we weight data so that the mean square of each waveform trace becomes the standard quantity. In this study, because we have a data set with multiple periodic ranges, weighting among different periodic ranges is also a problem. We weight data so that the total sensitivity of the whole data set of each periodic range becomes approximately equal. As described above, in contrast to previous studies, we rigorously compute $\mathbf{A}$ in eq. (4) without using any approximations other than the truncation of the basis.

To determine the model parameters $\boldsymbol{\delta}\mathbf{m}$ from eq. (3) we need some criteria. In this study we impose the following criteria:

$$\frac{1}{{\sigma_d}^2} \mid \mathbf{A}\,\boldsymbol{\delta}\mathbf{m} - \boldsymbol{\delta}\mathbf{d} \mid^2 + g^2 = \min, \tag{5}$$

where σ_d is the standard error of the observed data $\boldsymbol{\delta}\mathbf{d}$, and g is the weighted gradient of the model. The explicit form of g is given as follows:

$$\begin{aligned} g^2 \;=\; & \frac{1}{{\sigma_h}^2}\,\mathbf{H}^T_{\rm mantle}\mathbf{H}_{\rm mantle}\;\boldsymbol{\delta}\mathbf{m} + \frac{1}{{\sigma_r}^2}\,\mathbf{D}^T_{\rm mantle}\mathbf{D}_{\rm mantle}\;\boldsymbol{\delta}\mathbf{m} \\ & + \frac{1}{{\sigma_h'}^2}\,\mathbf{H}^T_{\rm crust}\mathbf{H}_{\rm crust}\;\boldsymbol{\delta}\mathbf{m} \;+ \frac{1}{{\sigma_r'}^2}\,\mathbf{D}^T_{\rm crust}\mathbf{D}_{\rm crust}\;\boldsymbol{\delta}\mathbf{m}, \end{aligned} \tag{6}$$

where σ_h and σ_r are the *a priori* standard error of the horizontal and the vertical smoothness for the mantle structure, respectively, σ_h' and σ_r' are those for the crustal structure, $\mathbf{H}_{\rm mantle}$ and $\mathbf{H}_{\rm crust}$ are the first order differential operator in the horizontal direction for the mantle and crustal region, respectively, and $\mathbf{D}_{\rm mantle}$ and $\mathbf{D}_{\rm crust}$ are the second order differential operator in the radial direction for the mantle and crustal region, respectively. Note that we assume a different standard error for the mantle and crustal structure. The solution $\boldsymbol{\delta}\mathbf{m}$ for the least square problems of eqs. (3)-(6) can be obtained by using the standard least square solution. In the solution, we should specify ${\sigma_h}^2/{\sigma_d}^2$, ${\sigma_r}^2/{\sigma_d}^2$, and ${\sigma_{h'}}^2/{\sigma_d}^2$ as the damping factors. Note that ${\sigma_{r'}}^2/{\sigma_d}^2$ is not required because we use the box car function as $X^{(k)}$ in eq. (1) to expand the heterogeneity in the crust and cannot represent radial dependency. We assumed ${\sigma_{h'}}^2 = 20{\sigma_h}^2$ because of the highly heterogeneous nature of the crust and then empirically determined the damping factors.

3 Results

3.1 Consistency in Overall Features

Figure 3 shows the lateral sections of the SH velocity model, SH18CE, obtained by this study. The color scale for each section is normalized by the maximum amplitude of the heterogeneity at that depth. Therefore deep red and deep blue represent primary heterogeneity patterns for each depth. The degree 0 component of the model is removed in these plots (the absolute amplitude of degree 0 is below 0.11 % for every section except for the section at 1210 km where the amplitude is -0.186%). As we see below, the overall features of SH18CE are consistent with those seen in previously obtained models.

At shallower depths we observe high velocity anomalies beneath the older continents and oceans and low velocity anomalies beneath the mid-ocean ridges and the island arcs, as has

been seen in most previous models. The depth of the older continents is one of the controversial problems. Gung *et al.* (2003) pointed out that the models constrained by SH waves tend to have thicker continental roots compared to the models constrained by SV waves. The model SH18CE also shows thicker continental roots. Comparing the models at 70 km and 280 km depths, we see strong high velocity anomalies at both depths beneath Eurasia, North America, Africa, and Australia. The exception is Brazil, where the high velocity anomalies seem to almost disappear at a depth of 280 km. These features are consistent with, for example, the model SAW24B16 by Mégnin & Romanowicz (2000). The discrepancies between the SH and SV models might be explained by the anisotropy at a depth of 250-400 km, as pointed out by Gung *et al.* (2003).

In the transition zone we observe high velocity anomalies presumably related to the subducting slabs, as seen in most previous models. Here we focus on the fate of the subducting slabs. At 530 km depth we widely observe high velocity anomalies beneath the Aleutian Islands and the Western Pacific. On the other hand, at 920 km depth we see high velocity anomalies only beneath Java, Mariana, Tonga, and Kamchatka, which indicates that the other slabs in this region stagnate in the vicinity of the 670 discontinuity. At 920 and 1210 km depths, we see clear high velocity anomalies beneath North and South America presumably related to the Farallon slab, and at 1210 km we see clear high velocity anomalies beneath India and the Bay of Bengal which is presumably related to the Tethys slab. These results are consistent with those obtained by detailed P delay time tomographies which are summarized in, for example, Fukao *et al.* (2001).

The change of the spectra of the lateral heterogeneities across the 670 km discontinuity is another important clue to the nature of the 670. In Figure 3 we see the predominance of larger wavelength heterogeneities at a depth of 530 km, whereas smaller wavelength heterogeneities predominate at 920 km. This result is consistent with the extensive studies on heterogeneity spectra in the mantle by Gu *et al.* (2001, 2003).

In the lowermost 1000 km of the mantle we see high velocity anomalies in the Circum-Pacific region and low velocity anomalies beneath Africa and the Pacific, as has been seen in most previous models. At the CMB we see two strong low velocity anomalies (colored deep red) beneath Africa and Pacific which widely extend in the horizontal directions. The lateral extent of these two anomalies is more or less equal. However, at 2390 km and 1940 km depths the lateral extent of the strong anomalies beneath Africa is much larger compared to that beneath the Pacific. This shows that we have definite differences between structures in these two major upwelling regions. These vertical sections are compared in the next subsection.

3.2 African and Pacific Upwelling System

In this subsection we compare low velocity anomalies beneath Africa and the Pacific. The thick blue lines in Figure 4a show the location of the vertical sections in Figures 4b and 4c. The heterogeneity pattern of the model SH18CE at the CMB and that of the input model used for the resolution tests in Figure 4c are overplotted on the right and the left in Figure 4a, respectively. The sections cut through the center of the strong low velocity anomalies. Figure 4b shows the model SH18CE beneath Africa and the Pacific for these sections. The results clearly show the difference of these two upwelling systems. The strong low velocity anomalies (indicated by orange or deep red; lower than -0.82%) beneath the Pacific are restricted to approximately the lowermost 300-400 km, whereas those beneath Africa extend for about 1300-1400 km from the CMB.

The strong low velocity regions beneath Africa are indicated based on extensive analysis of data from the South African Array and Tanzanian Array (e.g., Ritsema *et al.* 1998; Ni *et al.* 2002, 2005; Ni & Helmberger 2003abc). The anomalous region is estimated to extend from the CMB about 1200-1500 km up into the mantle, which is generally consistent with the results of

this study. The low velocity anomalies are estimated to be as low as approximately −3%, which is significantly larger than those obtained in this study. This discrepancy is probably due to the damping effect in the inversion conducted in this study. A ridge-like structure with sharp side boundaries has been reported, which is also generally consistent with this model. The detailed shape of the anomalous region seems to be a bit different: a large low velocity block (1200-1500 km high) tilted eastward has been reported, whereas a large low velocity block (800-900 km high) with a small low velocity block located on its upper-eastern boundary is observed in this study. This discrepancy might be due to the different resolution of the data sets used, and it is an important future research topic to check the compatibility of the model in this study with the data sets from the South African and Tanzanian Array.

On the other hand, the depth of the strong low velocity anomalies beneath the Pacific is relatively unknown. This is due mainly to the lack of array data which sample the whole of these low velocity anomalies. However, the results of this study seem to be consistent with the results obtained by regional array analysis. Data from the North American networks for Fiji-Tonga events are the most extensively studied in this region. These data sample the eastern part of the low velocity region. Several velocity models have been proposed, including those of Ritsema *et al.* (1997), Russell *et al.* (2001), and Avants *et al.* (2006). There exist some differences among these models, but all of them show strong low S velocity anomalies in the lowermost 300 km of the mantle (see Fig. 1 of Avants *et al.* 2006), which is consistent with the results of this study. Data from the Japanese networks for Fiji-Tonga events are also extensively studied. These data sample some of the western part of the low velocity region. However, because of the geometrical distribution of events and stations, the data have large variations in azimuths but small variations in epicentral distances. Constraining the vertical velocity profiles is thus difficult, and most of the previous studies have constrained only the location and the contrast of discontinuities by analyzing scattering waves. Among these studies, Kito *et al.* (2004) recently suggested that there exists a strong negative velocity jump in S wave velocity at 350 km from the CMB. If we assume that the region between this discontinuity and the CMB is the strong low velocity region, this result is consistent with the results obtained by this study.

The difference in the structure of SH18CE beneath Africa and the Pacific is not likely due to the different resolution between these regions. Figure 4c shows the results of the resolution tests. The bottom four sections in Figure 4c show the resultant output models computed by convolving the resolution kernels of SH18CE and the input models. The laterally dependent part of the input model (shown in the right in Fig. 4a) is defined so as to mimic the primary low velocity anomaly pattern of SH18CE at the CMB. The vertically dependent part of the model is tested for two cases: one is the case when the strong low velocity anomalies are restricted to 350 km from the CMB and the other is the case when they extend for 1350 km from the CMB. The amplitude of the low velocity anomalies in the input model is −3%. The vertical sections of the input and the resultant output models for the former case are shown in the first and the third sections from the left in Figure 4c, and those for the latter case are shown in the second and the last sections. Because of the limited resolution, the output model has heterogeneities with smaller amplitudes in broader regions than does the input model. However, the resolutions beneath both Africa and the Pacific are sufficient to distinguish the differences between these two cases. This suggests that the observed differences of the structure beneath Africa and the Pacific are reliable.

3.3 Stagnant Slabs in the Western Pacific Region

In Figure 3 we see that the overall subducting style observed in SH18CE is generally consistent with the previous results. Fukao *et al.* (2001) showed that the slabs around Japan (from the South Kuril to the Izu-Bonin region) stagnate on the 670 discontinuity. Here we compare their

detailed structures and confirm further agreements. We choose the four vertical sections shown in Figure 5. We compare the short wavelength P model, WEPP2, by Obayashi *et al.* (1997) and SH18CE. Figure 6 shows the result.

WEPP2 clearly shows the stagnant slabs on the 670 discontinuity, which appears to be a consistent feature among recent short wavelength P models. WEPP2 also shows further detailed features. If we focus on the depth of the strongest high velocity anomalies within the stagnant slabs, we see variations region by region. The highest velocity anomaly is in the shallower part of the transition zone for the S-Kuril and Japan-A section, whereas it is in the deeper part of the transition zone for the Izu-Bonin section. Although there should be debate on the reliability of such a detailed structure, it is notable that similar features can be observed in the model obtained by this study. SH18CE shows the high velocity anomalies in the transition zone in each section. SH18CE also shows the depth variations of the highest velocity anomalies: the depths for the S-Kuril and Japan-A sections seem to be shallower than that for the Izu-Bonin section.

This agreement does not appear to be a common feature among recent long wavelength S models. Figure 7 shows the models SAW24B16 (Mégnin & Romanowicz 2000), S20RTS (Ritsema *et al.* 1999), SB4L18 (Masters *et al.* 2000), and S362D1 (Gu *et al.* 2001) for the vertical sections shown in Figure 5. We can confirm that the strong high velocity anomalies in the transition zone are observed in every model. However, the depth variations of the highest anomalies are not well observed, indicating these variations are a unique agreement observed only in WEPP2 and SH18CE.

Figure 8 shows which heterogeneity patterns in the lateral section produce these depth variations. At a depth of 530 km we see strong high velocity anomalies which extend widely over the subduction zones and some of the continental regions. On the other hand, at 670 km such strong anomalies disappear beneath the Japan Sea, Far East Russia, and North East China. This suggests that the strong high velocity anomalies are absent at the base of the transition zone in these regions. This does not seem to be an artifact due to the lack of resolution. Figure 9 shows the results of the resolution tests. We consider two input models. One of them has the same heterogeneity pattern at 530 and 670 km, as shown at the left of Figure 9a. The other has a different heterogeneity pattern at the two depths, as shown at the left of Figure 9b. The results (shown at the right of Figs. 9a and 9b) indicate that we can resolve the lack of high velocity anomalies at the base of the transition zone. This suggests that the observed depth variations of the highest velocity anomalies within the stagnant slabs are reliable.

4 Conclusion and Future Topics

A whole mantle SH velocity model is obtained from an independent data set which fully includes the later phase information. The model is obtained by using a waveform inversion technique based on 3D Born kernels. The resultant model clearly shows the difference in structure between the two major upwelling systems beneath Africa and the Pacific. The strong low velocity anomalies beneath Africa extend for 1300-1400 km from the CMB, whereas those beneath the Pacific are restricted to the lowermost 300-400 km of the mantle. These features are generally consistent with the results obtained by previous array analyses.

The detailed structures of stagnant slabs around Japan are compared to the short wavelength P model, WEPP2 (Obayashi *et al.* 1997). The results show the depth variations of the highest velocity anomaly within the stagnant slabs. Comparisons to recent long wavelength S models are also conducted, and we confirm that the strong high velocity anomalies in the transition zone are a common feature among recent long wavelength S models. However, the depth variations of the highest velocity anomaly are not prominent, which indicates that these variations in a long wavelength S model are a unique feature obtained by this study.

In this study we conducted rigorous inversion under the assumptions of eq. (3): linear dependency between the observed data $\boldsymbol{\delta}\mathbf{d}$ and the model parameters $\boldsymbol{\delta}\mathbf{m}$ is assumed. Because of the non-linear nature of waveform inversion, inclusion of the non-linearity effects is an important future topic. Li & Romanowicz (1995) introduced the non-linear asymptotic coupling theory to be able to compute nonlinear phase perturbations due to the averaged heterogeneities between the source and the receiver. Takeuchi *et al.* (2000) introduced improved higher order Born approximations which ensures convergence. Applying such methods to compute 3D kernels for the whole mantle structure should be a challenging future research topic.

Acknowledgments

We are grateful for the use of the SGI LX3700 at the Earthquake Research Institute, University of Tokyo, the SR8000/MPP at the Information Technology Center, University of Tokyo, and the Earth Simulator at the Earth Simulator Center of the Japan Marine Science and Technology Center. This research was partly supported by grants from the Japanese Ministry of Education, Culture, Sports, Science, and Technology (Nos. 16740249 and 16075208).

References

Avants, M., Lay, T., Russell, S.A. & Garnero, E.J., Shear velocity variation within the D" region beneath the central Pacific, *J. geophys. Res.*, **111**, B05305, doi:10.1029/2004JB003270.

Bassin, C., Laske, G. & Masters, G., 2000. The current limits of resolution for surface wave tomography in North America, *EOS Trans. AGU*, **81**, Fall Meet. Suppl., Abstract S12A-03.

Bijwaard, H., Spakman, W. & Engdhal, E.R., 1998. Closing the gap between regional and global travel time tomography, *J. geophys. Res.*, **103**, 30,055–30,078.

Cummins, P.R., Geller, R.J., Hatori, T. & Takeuchi, N., 1994. DSM complete synthetic seismograms: SH, spherically symmetric, case, *Geophys. Res. Lett.*, **21**, 533–536.

Dziewonski, A.M. & Anderson, D. L., 1981. Preliminary reference Earth model, *Phys. Earth planet. Int.*, **25**, 297–356.

Fukao, Y., Widiyantoro, S. & Obayashi, M., 2001. Stagnant slabs in the upper and lower mantle transition region, *Rev. Geophys.*, **39**, 291–323.

Geller, R.J. & Ohminato, T., 1994. Computation of synthetic seismograms and their partial derivatives for heterogeneous media with arbitrary natural boundary conditions using the Direct Solution Method, *Geophys. J. Int.*, **116**, 421–446.

Geller, R.J. & Takeuchi, N., 1995. A new method for computing highly accurate DSM synthetic seismograms, *Geophys. J. Int.*, **123**, 449–470.

Grand, S.P., 2002. Mantle shear-wave tomography and the fate of subducted slabs, *Phil. Trans. R. Soc. Lond. A*, **360**, 2475–2491.

Gu, Y.J., Dziewonski A.M., Su W.-J. & Ekstrøm, G., 2001. Models of the mantle shear velocity and discontinuities in the pattern of lateral heterogeneities, *J. geophys. Res.*, **106**, 11,169–11,199.

Gu, Y.J., Dziewonski A.M. & Ekstrøm, G., 2003. Simultaneous inversion for mantle shear velocity and topography of transition zone discontinuities, *Geophys. J. Int.*, **154**, 559–583.

Gung, Y., Panning, M. & Romanowicz, B., 2003. Global anisotropy and the thickness of continents, *Nature*, **422**, 707–711.

Hara, T., 2004. Waveform inversion for 3-D earth structure using the Direct Solution Method implemented on vector-parallel supercomputer, *Phys. Earth planet. Int.*, **146**, 65–74.

Kawai, K., Takeuchi, N. & Geller, R.J., 2006. Complete synthetic seismograms up to 2 Hz for transversely isotropic spherically symmetric media, *Geophys. J. Int.*, **164**, 411–424.

Kito, T., Krüger, F. & Negishi, H., 2004. Seismic heterogeneous structure in the lowermost mantle beneath the southwestern Pacific, *J. Geophys. Res.*, **109**, B09304, doi:10.1029/2003JB002677.

Li, X.D. & Romanowicz, B., 1995. Comparison of global waveform inversions with and without considering cross-branch modal coupling, *Geophys. J. Int.*, **121**, 695–709.

Li, X.D. & Tanimoto, T., 1993. Waveforms of long-period body waves in a slightly aspherical Earth model, *Geophys. J. Int.*, **112**, 92–102.

Love, A.E., 1927, *A Treatise on the Mathematical Theory of Elasticity*, Cambridge University Press, Cambridge.

Masters, G., Laske, G., Bolton, H. & Dziewonski, A., 2000. The Relative Behavior of Shear Velocity, Bulk Sound Speed, and Compressional Velocity in the Mantle: Implications for Chemical and Thermal Structure, *Earth's Deep Interior: Mineral Physics and Tomography From the Atomic to the Global Scale*, edited by S. Karato, A.M. Forte, R.C. Liebermann, G. Masters & L. Stixrude, 63–87.

Mégnin, C. & Romanowicz, B., 1999. The effects of the theoretical formalism and data selection on mantle models derived from waveform tomography, *Geophys. J. Int.*, **138**, 366–380.

Mégnin, C. & Romanowicz, B., 2000. The three-dimensional shear velocity structure of the mantle from the inversion of body, surface and higher-mode waveforms, *Geophys. J. Int.*, **143**, 709–728.

Montelli, R., Nolet, G., Dahlen, F.A., Masters, G., Engdahl, E.R. & Hung, S.H., 2004, Finite-frequency tomography reveals a variety of plumes in the mantle, *Science*, **303**, 338–343.

Ni, S.D., Tan, E., Gurnis, M. & Helmberger, D.V., 2002. Sharp sides to the African superplume, *Science*, **296**, 1850–1852.

Ni, S.D. & Helmberger, D.V., 2003a. Ridge-like lower mantle structure beneath South Africa, *J. geophys. Res.*, **108**, 2094, doi:10.1029/2001JB001545.

Ni, S.D. & Helmberger, D.V., 2003b. Seismological constraints on the South African superplume; could be the oldest distinct structure on Earth, *Earth planet. Sci. Lett.*, **206**, 119–131.

Ni, S.D. & Helmberger, D.V., 2003c. Further constraints on the African superplume structure, *Phys. Earth planet. Int.*, **140**, 243–251.

Ni, S.D., Helmberger, D.V. & Tromp, J., 2005. Three-dimensional structure of the African superplume from waveform modelling, *Geophy. J. Int.*, **161**, 283–294.

Obayashi, M., Sakurai, T. & Fukao, Y., 1997. Comparison of recent tomographic models. *Proc. Int. Symp. on New Images of the Earth's Interior Through Long Term Ocean-Floor Observations*, edited by K. Suyehiro, Chiba, Nov. 6-8, 1997, p. 29.

Panning, M. & Romanowicz, B., 2006. A three-dimensional radially anisotropic model of shear velocity in the whole mantle, *Geophys. J. Int.*, **167**. 361–379.

Ritsema, J., Garnero, E.J. & Lay, T., 1997. A strongly negative shear velocity gradient and lateral variability in the lowermost mantle beneath the Pacific, *J. geophys. Res.*, **102**, 20,395–20,411.

Ritsema, J., Ni, S.D. & Helmberger, D.V., 1998. Evidence for strong shear velocity reductions and velocity gradients in the lower mantle beneath Africa, *Geophys. Res. Lett..*, **25**, 4245–4248.

Ritsema, J., van Heijst, H.J. & Woodhouse, H., 1999. Complex shear wave velocity structure imaged beneath Africa and Iceland, *Science*, **286**, 1925–1928.

Russell, S.A., Reasoner, C., Lay, T. & Revenaugh, J., 2001. Coexisting shear- and compressional-wave seismic velocity discontinuities beneath the central Pacific, *Geophys. Res. Lett.*, **28**, 2281–2284.

Takeuchi, N., 2005. Finite boundary perturbation theory for the elastic equation of motion, *Geophys. J. Int.*, **160**, 1044–1058.

Takeuchi, N. & Geller, R.J., 2003. Accurate numerical methods for solving the elastic equation of motion for arbitrary source locations, *Geophys. J. Int.*, **154**, 852–866.

Takeuchi, N., Geller, R.J. & Cummins, P.R., 1996. Highly accurate P-SV complete synthetic seismograms using modified DSM operators, *Geophys. Res. Lett.*, **23**, 1175–1178.

Takeuchi, N., Geller, R.J. & Cummins, P.R., 2000. Complete synthetic seismograms for 3-D heterogeneous Earth models computed using modified DSM operators and their applicability to inversion for Earth structure, *Phys. Earth Planet. Int.*, **119**, 25–36.

Takeuchi, N. & Kobayashi, M., 2004. Improvement of seismological earth models by using data weighting in waveform inversion, *Geophys. J. Int.*, **158**, 681–694.

van der Hilst, R.D., Widiyantro, S. & Engdahl E.R., 1997. Evidence of deep mantle circulation from global tomography, *Nature*, **386**, 578–584.

Woodhouse, J.H., 1980. The coupling and attenuation of nearly resonant multiplets in the Earth's free oscillation spectrum, *Geophys. J. R. astr. Soc.*, **61**, 261–283.

Woodhouse, J.H. & Dziewonski, A.M., 1984. Mapping the upper mantle: three-dimensional modeling of Earth structure by inversion of seismic waveforms, *J. geophys. Res.*, **89**, 5953–5986.

Figure Captions

Figure 1: An example of selected time windows chosen as a data set. The transverse component of the data at the station OBN (the epicentral distance is 59.9°) for the Japan Sea event on 07/21/94 (the centroid depth is 489.1 km and the moment magnitude is $M_{\rm W} = 7.3$) are used for this example. Selected time windows (shown in black boxes) are shown with observed waveform data (shown in red lines) and synthetic seismograms (shown in green lines) for the periodic range of (a) 200-400 sec, (b) 100-200 sec, and (c) 50-100 sec.

Figure 1: (continued)

Figure 2: Sensitivity distribution at the CMB for the data set used in this study (left) and the data set excluding data after the arrival of G1 for the periodic range of 50-100 sec (right). The color scale is linearly attributed according to the logarithm of the sensitivity. Sensitivity is defined by the ratio to the minimum sensitivity appearing in these two maps.

Figure 3: SH velocity structure obtained in this study at various depths. The color scale is normalized by the maximum amplitude of the heterogeneities at each depth.

Figure 3: (continued)

Figure 4: (a) The location of the vertical sections shown in Figures 4b and 4c (thick blue lines). The heterogeneity pattern of SH18CE at the CMB and that of the input model used in the resolution test in Figure 4c are overplotted on the right and the left figure, respectively. (b) Vertical sections of SH18CE for the sections beneath Africa (left) and the Pacific (right). The color scale is saturated if the heterogeneity exceeds -2.0% or 2.0%. (c) The vertical sections of the input models (upper) and the resultant output model computed by convolving the resolution kernels of SH18CE and the input models (lower). The sections beneath Africa (the left two) and beneath Pacific (the right two) are shown, respectively. Two input models are tested. One is the case when the strong low velocity anomalies in the input model are restricted to 350 km from the CMB (the first and the third sections from the left) and the other is the case when they extend for 1350 km from the CMB (the second and the last sections from the left). The color scale is saturated if the heterogeneity exceeds -2.0% or 2.0%.

Figure 5: The location of the vertical sections shown in Figures 6 and 7 (thick blue lines). The section names are overplotted.

Figure 6: The vertical sections of WEPP2 (Obayashi *et al.* 1997; upper) and SH18CE (lower) for the four sections shown in Figure 5. The color scale is saturated if the heterogeneity exceeds -2.0% or 2.0%.

Figure 7: The vertical sections of SAW24B16 (Mégnin & Romanowicz 2000), S20RTS (Ritsema *et al.* 1999), SB4L18 (Masters *et al.* 2000), and S362D1 (Gu *et al.* 2001) for the four sections shown in Figure 5. The color scale is saturated if the heterogeneity exceeds -2.0% or 2.0% except for SAW24B16. For SAW24B16 the color scale is saturated if the heterogeneity exceeds -3.0% or 3.0%.

Figure 8: Enlarged lateral sections of SH18CE around Japan at 530 and 670 km depths. The strong high velocity anomalies are absent at 670 km beneath the Japan Sea, Far East Russia, and North East China.

Figure 9: (a) Lateral sections of the input model (left) and the resultant output model computed by convolving the resolution kernels and the input model (right) at depths of 530 km (upper) and 670 km (lower). The case when the input model has the same heterogeneity pattern at depths of 530 and 670 km is tested. (b) Identical to (a) except that the case when the input model has different heterogeneity patterns at depths of 530 and 670 km is tested.

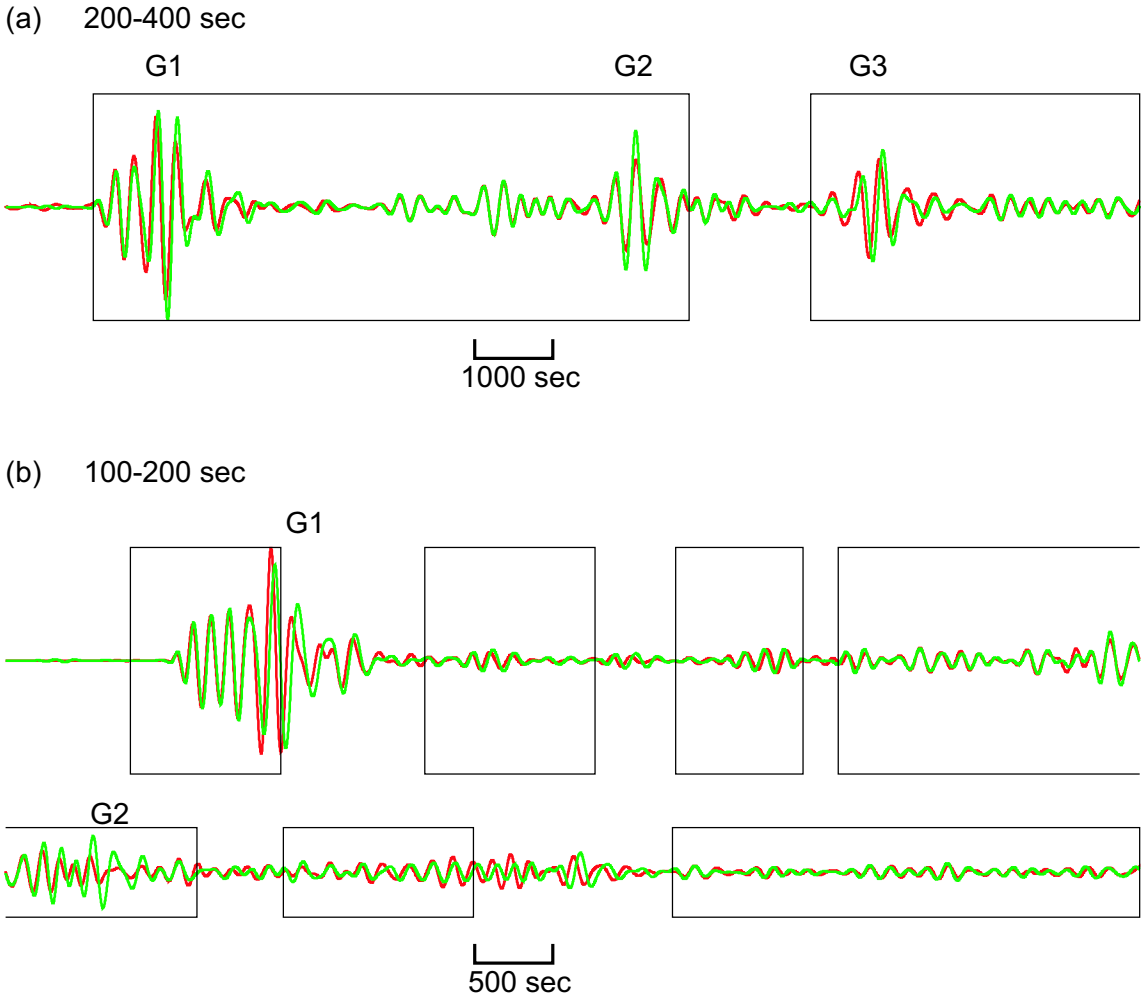

Figure 1

(c) 50-100 sec

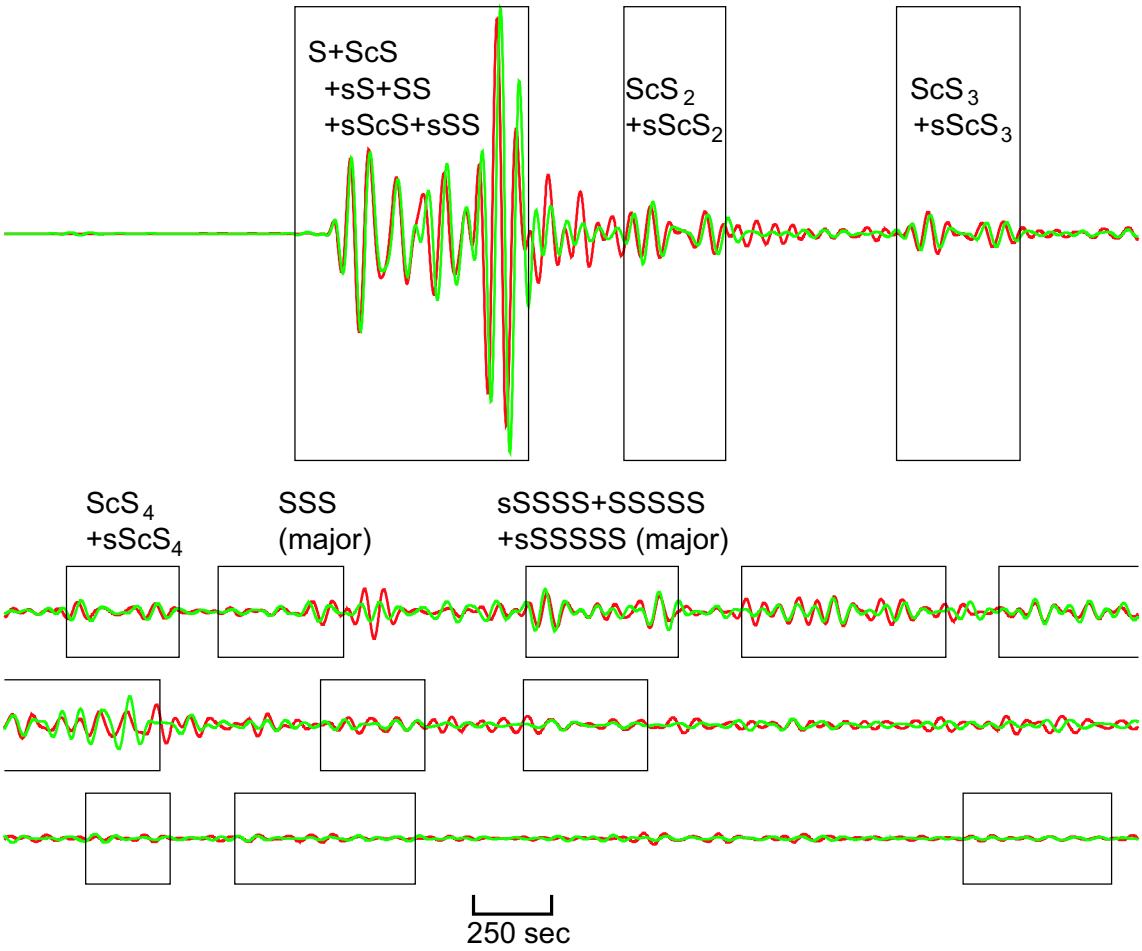

Figure 1 (continued)

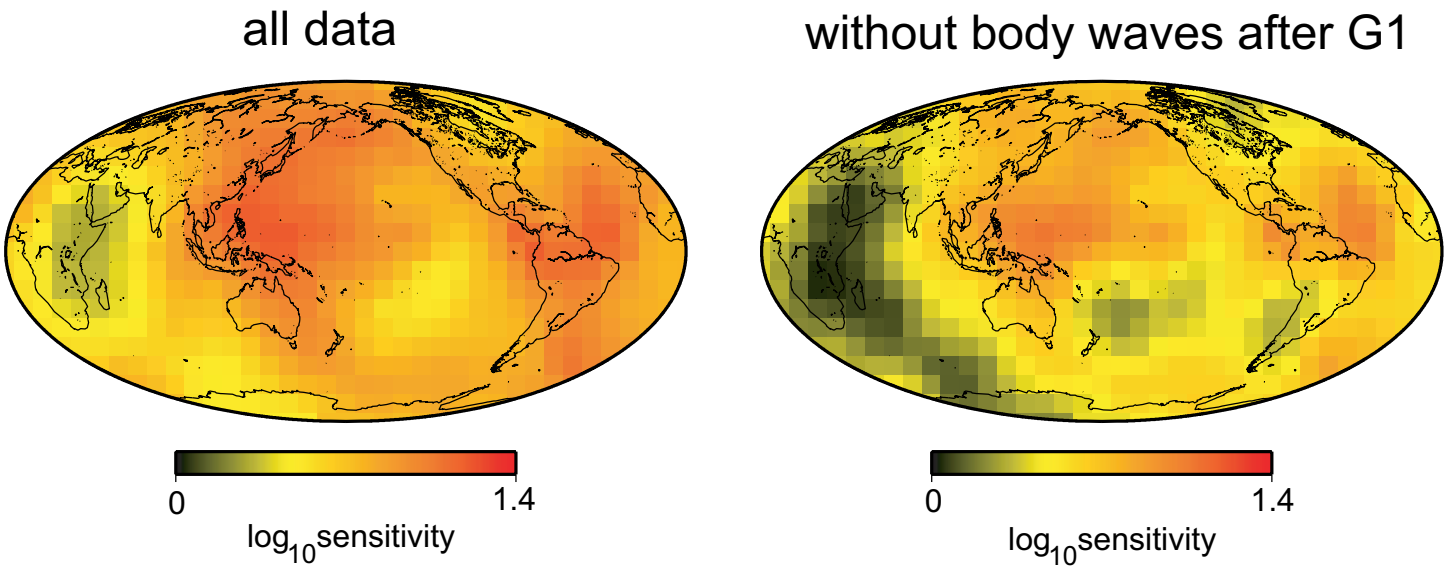
all data
0
1.4
log10sensitivity
without body waves after G1
0
1.4
log10sensitivity

Figure 2

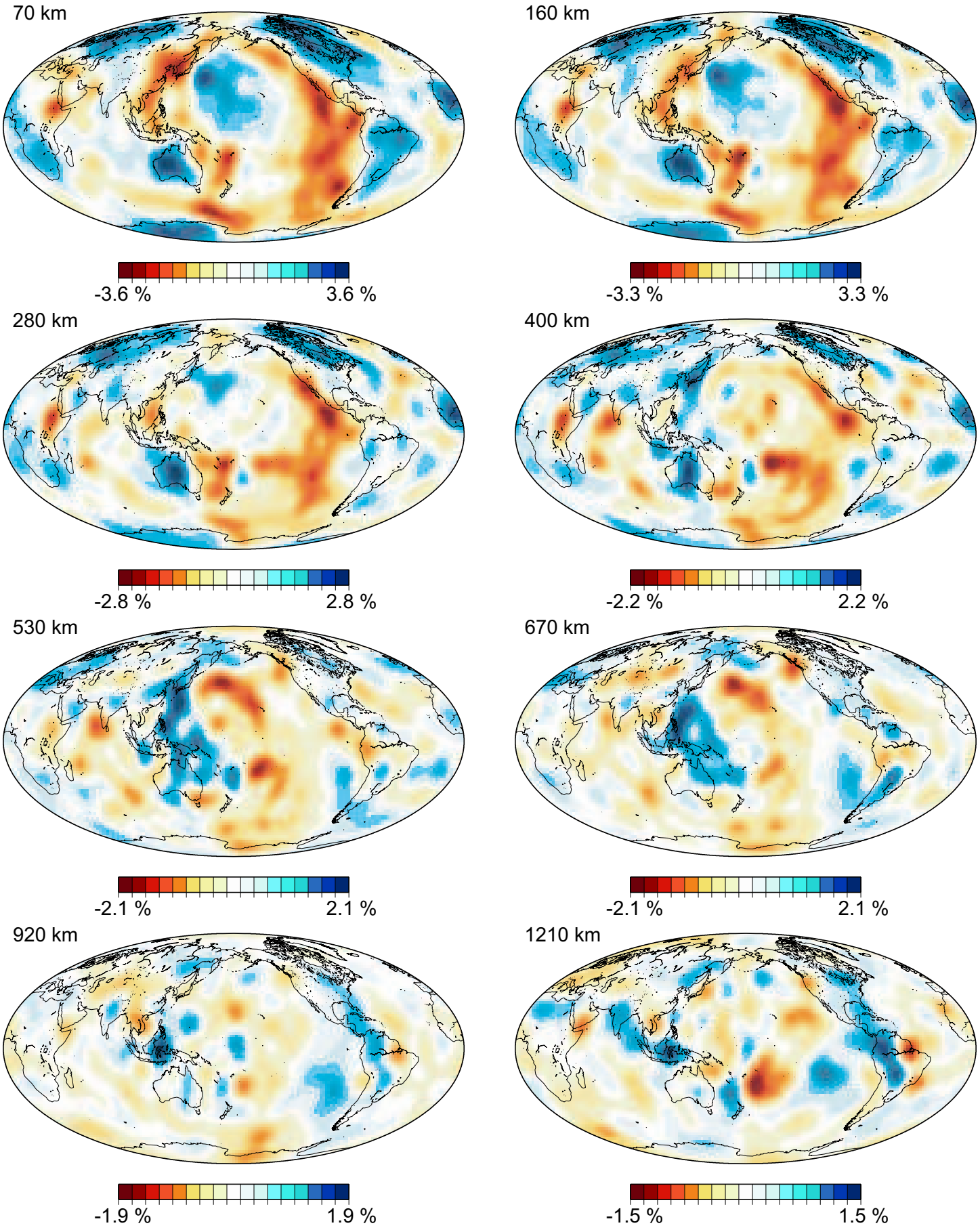
70 km
-3.6 %
3.6 %
160 km
-3.3 %
3.3 %
280 km
-2.8 %
2.8 %
400 km
-2.2 %
2.2 %
530 km
-2.1 %
2.1 %
670 km
-2.1 %
2.1 %
920 km
-1.9 %
1.9 %
1210 km
-1.5 %
1.5 %

Figure 3

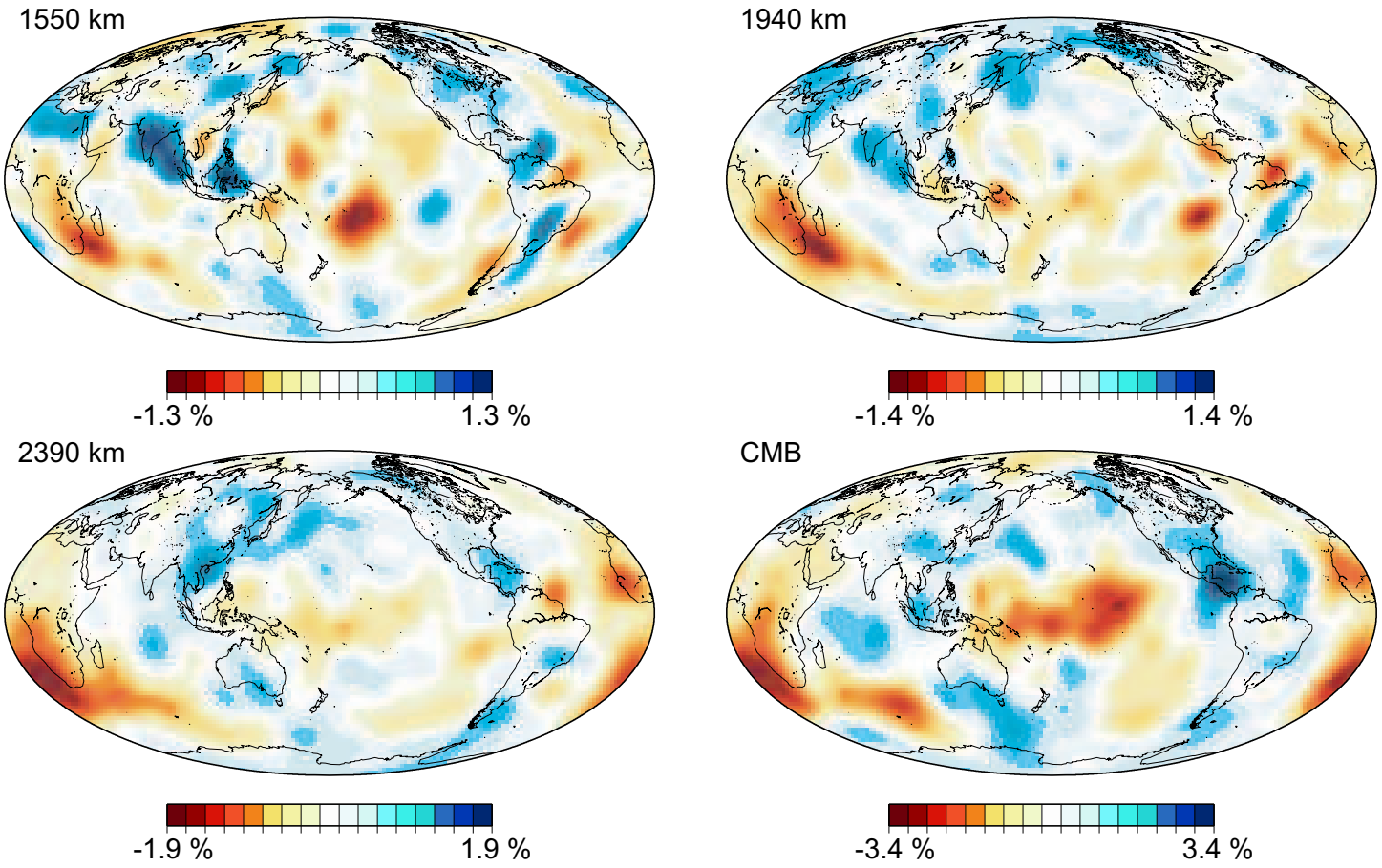

Figure 3 (continued)

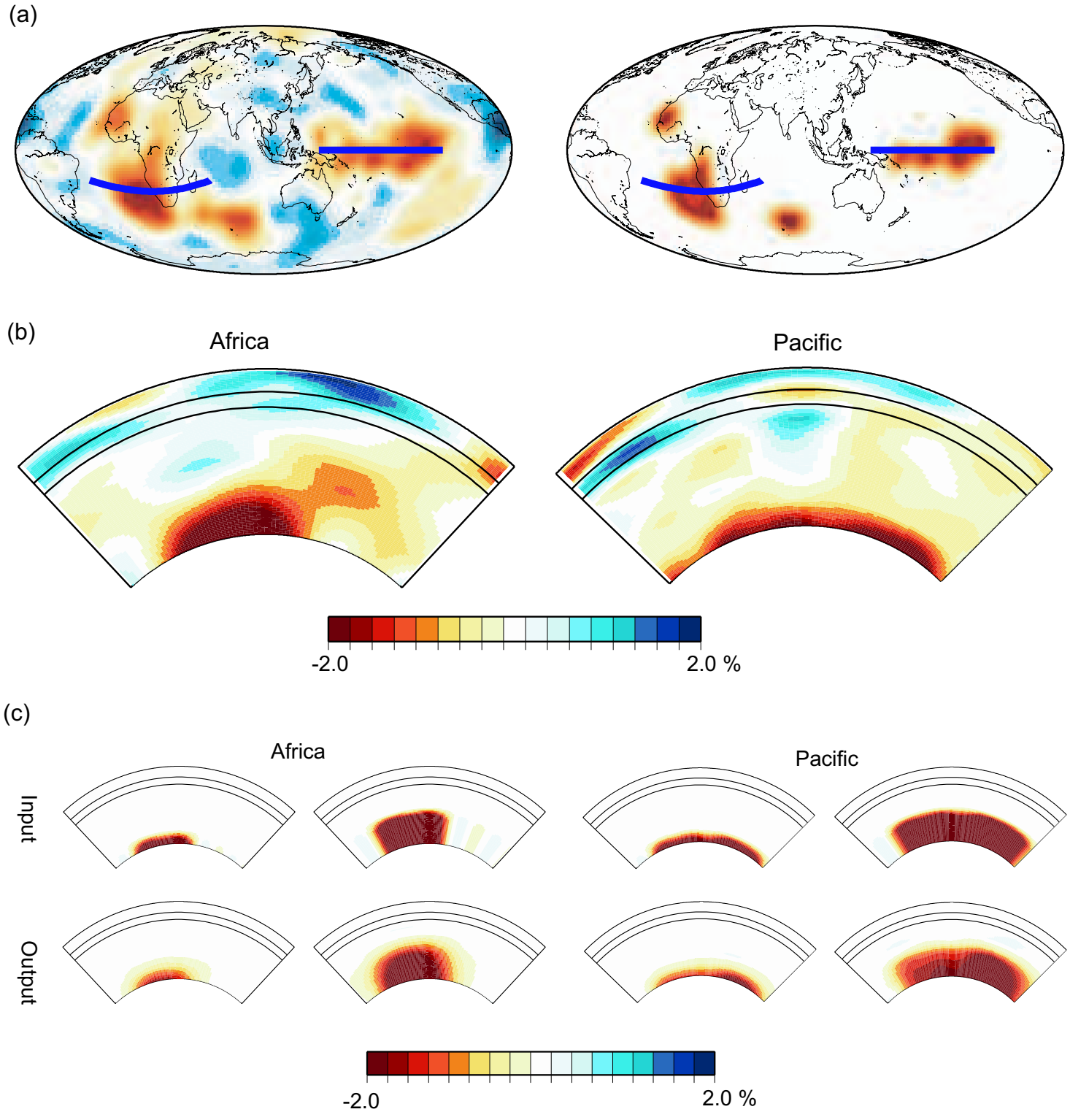

Figure 4

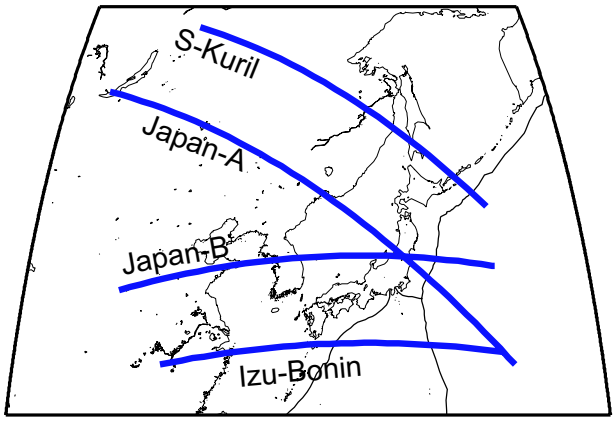

Figure 5

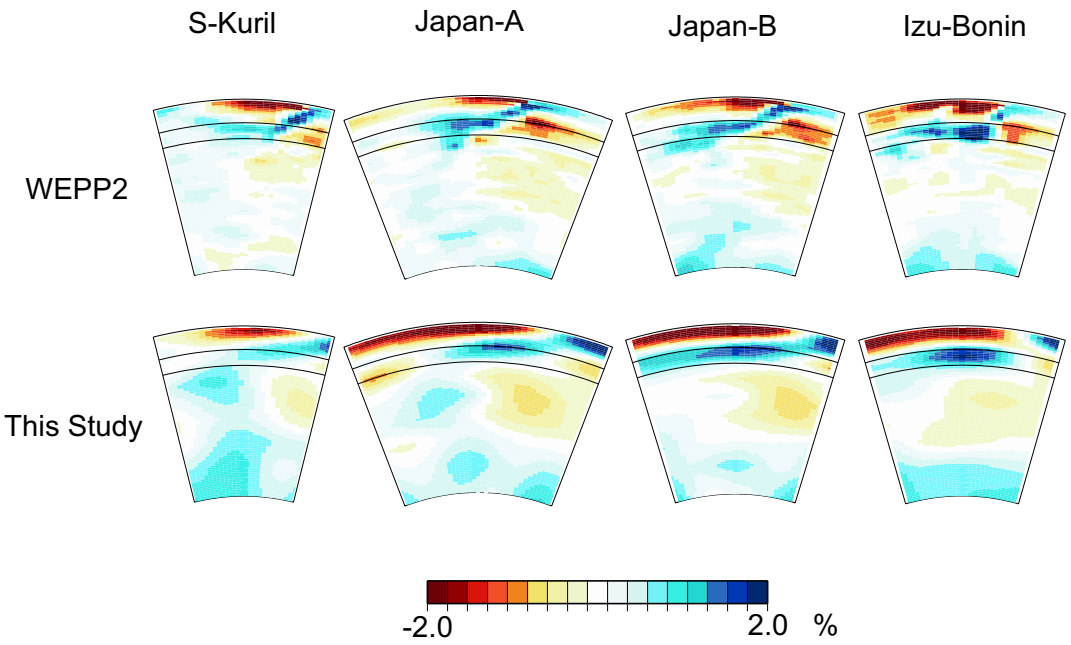

Figure 6

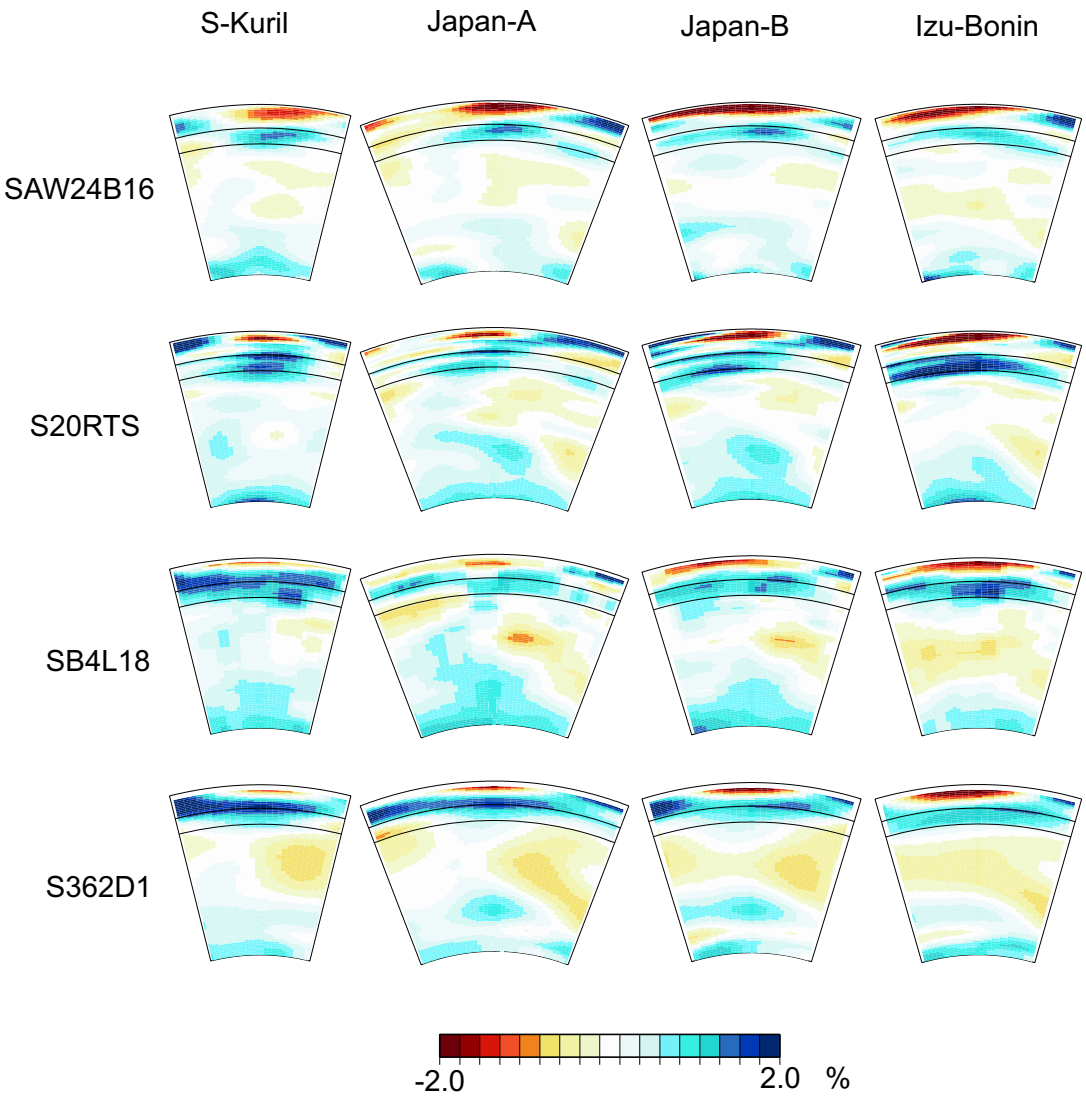
S-Kuril
Japan-A
Japan-B
Izu-Bonin
SAW24B16
S20RTS
SB4L18
S362D1
-2.0
2.0
%

Figure 7

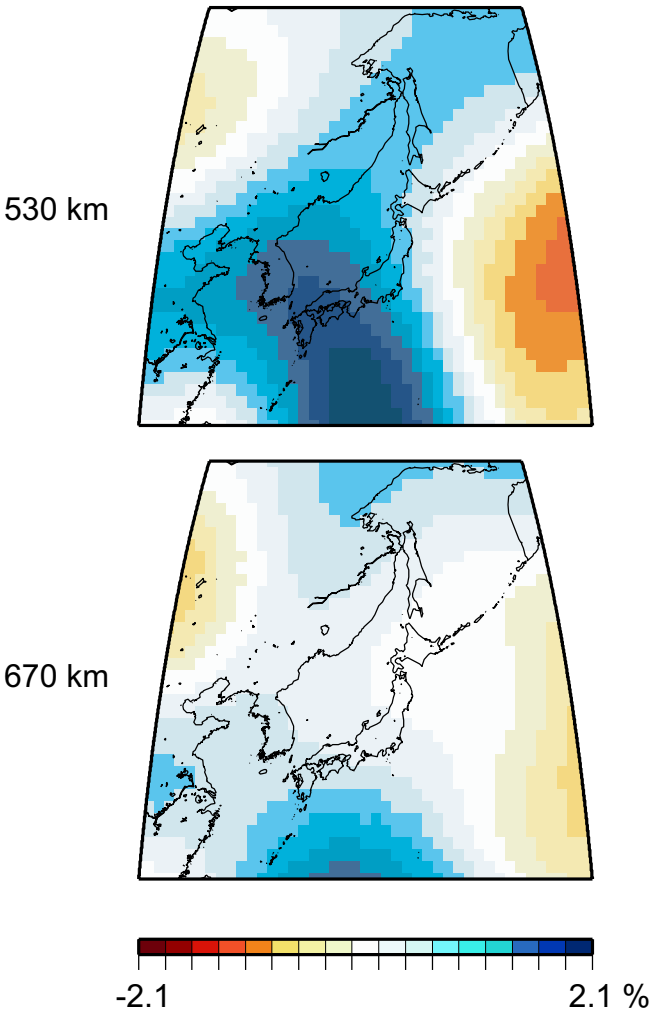

Figure 8

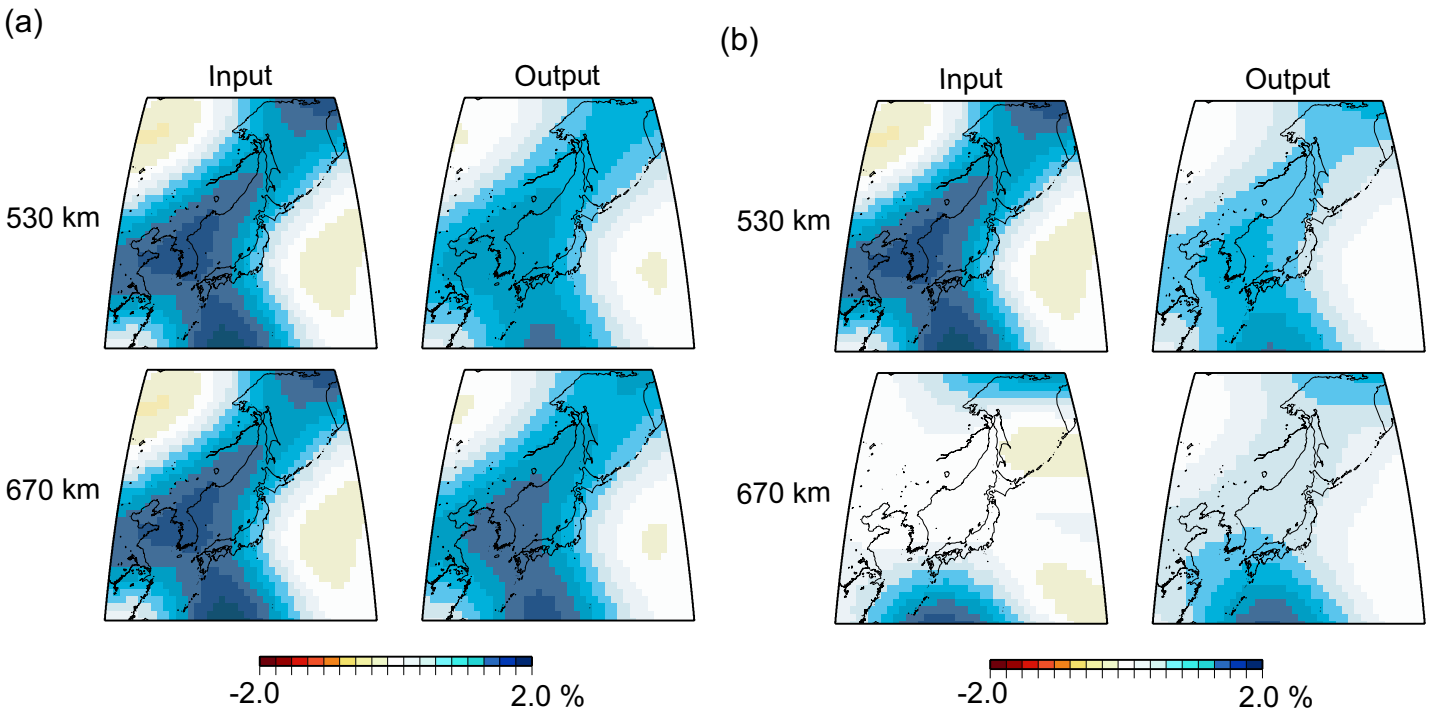
(a)
Input
Output
530 km
670 km
-2.0
2.0 %
(b)
Input
Output
530 km
670 km
-2.0
2.0 %

Figure 9